Supplementary Materials

Spin State Modulation of MnO_2 by Zn-Doping for Enhanced Supercapacitor and Hydrogen Evolution

Juyin Liu [1], Xue Zhang [2], Xuefeng Wu [1], Jingping Hai [1], Xiyuan Li [1], Ruming Feng [1,*] and Yanfang Gao [2,*]

[1] Inner Mongolia Daqingshan Laboratory, Hohhot 017000, China
[2] School of Chemical Engineering, Inner Mongolia University of Technology, Hohhot 010051, China
* Correspondence: 459159374@qq.com (R.F.); yf_gao@imut.edu.cn (Y.G.)

1. Materials

All chemicals used in the experiment were analytical grade with no further purification. Potassium permanganate ($KMnO_4$, ≥98%) was purchased from Tianjin Damao Chemical Reagent Co., Ltd. Manganese sulfate monohydrate ($MnSO_4·H_2O$, ≥99%), Zinc sulfate heptahydrate ($ZnSO_4·7H_2O$, AR), Potassium hydroxide (KOH, ≥85%), Lithium sulphate ($Li_2SO_4·H_2O$, ≥99%) was purchased from Aladdin Reagent (Shanghai) Co., Ltd. Nickel foam (NF) was purchased from Taiyuan Lizhiyuan Technology Co., Ltd. Acetone and HCl were provided by Tianjin Kemeng Chemical Industry & Trade Co.

2. Characterization Methods

The morphology and microstructure of the samples were marked using scanning electron microscopy (SEM, Zeiss sigma 300) and transmission electron microscopy (TEM, FEI Tecnai F20, 200 kV). The chemical composition and element mapping analysis of samples were confirmed by an energy dispersive X-ray spectrometer (EDS) attached to the SEM. X-ray photoelectron spectroscopy (XPS, Thermo Fisher ESCALAB 250Xi) was used to determine the electronic states of the samples, and all spectra were standardized with the C 1s peak of the non-constant carbon at 284.8 eV. Raman spectra (Thermo Fisher Scientific, 532 nm YAG laser) were recorded. X-ray diffraction (XRD-6100, Shimadzu) was used to study the phase and crystal structure of the materials with a Cu Ka (λ = 1.5405 Å) radiation source (40 kV and 30 mA) at a scan rate of 10° min^{-1}, working in the angular range of 5–80°. Electron paramagnetic resonance (EPR) was carried out to quantify oxygen vacancies with a Bruker A300, operating para meters were 9853 MHz, 20.03 mW. Temperature-dependent magnetic susceptibility measurements were performed in the temperature range from 2 to 300 K with a magnetic field of 1000 Oe on a physical property measurement system (PPMS-9, Quantum Design). The magnetic field range of the M-H curve is −20,000 to 20,000 Oe at 300 K.

3. Electrochemical Measurements

The supercapacitor performance of C-Zn-MnO_2 electrode materials was first tested in the three-electrode system. The Ag/AgCl electrode was the reference electrode, the Pt mesh was used as the counter electrode, and the C-Zn-MnO_2 electrodes were the working electrode (the working electrode was prepared by loading about 1 mg or so of active material between 1×1 cm^2 of nickel foam (NF), and pressed down for 15 s using a pressure of 10 Mpa without the addition of any conductive agent or binder). In the catalytic testing system, a graphite rod and a Ag/AgCl (saturated KCl) electrode were used as the counter electrode and the reference electrode. In addition, 1 M KOH served as an electrolyte for catalytic research. The NF coated with catalyst, 5 mg of the catalyst and 20 mL of Nafion solution (5 wt%) were dispersed in 490 mL of DI and 490 mL of ethanol followed by sonicated for 40 min. Next, 100 mL of ink was dropped on the NF and left to dry. Then, Zn-MnO_2 was used as the positive electrode, and La-MoO_3/GQD previously prepared by our group was used as the negative electrode material (mass ratio of 0.91:1), and an asymmetric supercapacitor (ASC) of the 2032-coin type was assembled with Whatman glass fiber membrane. The electrolyte was 1 M Li_2SO_4 aqueous solution, with the voltage window ranging from 0–1.8 V.

All measurement methods were performed using a CHI760E electrochemical workstation (Shanghai Chenhua Instruments Co., Ltd., China), including cyclic voltammetry (CV), galvanostatic charge–discharge (GCD), linear sweep voltammetry (LSV) and electrochemical impedance spectroscopy (EIS). CV tests were

generally performed at scan rates of 10, 20, 30, 50, 80, 100, and 120 mV s^{-1}. EIS spectra were measured in the frequency range of 0.01–100 kHz with an alternate current amplitude of 5 mV at open circuit voltage. The specific capacitance was obtained by calculating according to Equation (S1):

$$C = \frac{I\Delta t}{m\Delta V} \quad (S1)$$

where C is the specific capacitance (F g^{-1}), I is the discharge current (A), m is the load mass of the active material (mg), Δt is the discharge time (s), and ΔV is the potential window (V).

Furthermore, the energy density (E, Wh kg^{-1}) and power density (P, W kg^{-1}) of the ASC device were calculated by Equations (S2) and (S3), respectively [1].

$$E = \frac{1}{2\times3.6} C\Delta V^2 \quad (S2)$$

$$P = 3600 \times \frac{E}{\Delta t} \quad (S3)$$

where C means the specific capacitance of the coin cell (F g^{-1}), and ΔV represents the voltage window (V), Δt is the discharge time (s).

Furthermore, all recorded potentials in electrocatalytic measurements were calibrated with the reversible hydrogen electrode (RHE) according to the Nernst equation. The RHE and values of overpotential were deduced as following (4) [2]:

$$E_{(RHE)} = E_{(Ag/AgCl)} + 0.197 + 0.059 \times pH \quad (S4)$$

LSV curves were used to measure the electrocatalytic activity of the catalyst at a scan rate of 5 mV s^{-1}, with all polarization curves 90% iR-compensated, where i is the current and R is the uncompensated electrolyte ohmic resistance measured by electrochemical impedance spectroscopy (EIS). The current density was calculated from the actual area of the prepared catalyst immersed in the electrolyte. According to the Tafel equation: $\eta = a + b\log j$, using the logarithm of the current density as the X-axis and the overpotential as the Y-axis, a Tafel plot is obtained, where a is the Tafel constant, b is the Tafel slope, j is the cathodic current density, and η is the overpotential.

4. Calculation of Lattice Strain

The lattice strain (S) can be calculated by the Equation (S5):

$$S = \left|\frac{c-c_0}{c_0}\right| \times 100\% \quad (S5)$$

where c is lattice parameter of MnO_2 and c_0 is lattice parameter of Zn-MnO_2.

The calculated S are shown in Table S1.

5. Calculation of e_g Filling

The effective magnetic moment (μ_{eff}) can be obtained based on the Langevin theory by the Equation (S6) [3]:

$$\mu_{eff} = \sqrt{8C}\mu_B \quad (S6)$$

where C is Curie constant and obtained from the fittings on the susceptibility (χ=M/H) above the paramagnetic transition temperatures by a Curie-Weiss law $\chi = C/(T-\theta)$, where θ is Curie-Weiss temperature. The μ_{eff} obtained can be used to calculate Equations (S7) and (S8) [4]:

$$\mu_{eff} = \mu_B g\sqrt{S_{LS}(S_{LS}+1)V_{LS}+S_{HS}(S_{HS}+1)V_{HS}} \quad (S7)$$

$$V_{LS}+V_{HS}=1 \quad (S8)$$

where g is the Landé factor, with g = 2. V_{HS} and V_{LS} represent the volume fractions of Mn^{3+} in the high-spin and low-spin states, respectively. S_{HS} is the number of electrons with unpaired up-spin, and S_{LS} is the number of electrons with unpaired down-spin. S_{LS} = 0 and S_{HS} = 2. The e_g filling (x) is obtained from Equation (S9):

$$x = V_{HS} \times S_{HS} \quad (S9)$$

The calculated e_g fillings are shown in Table S2.

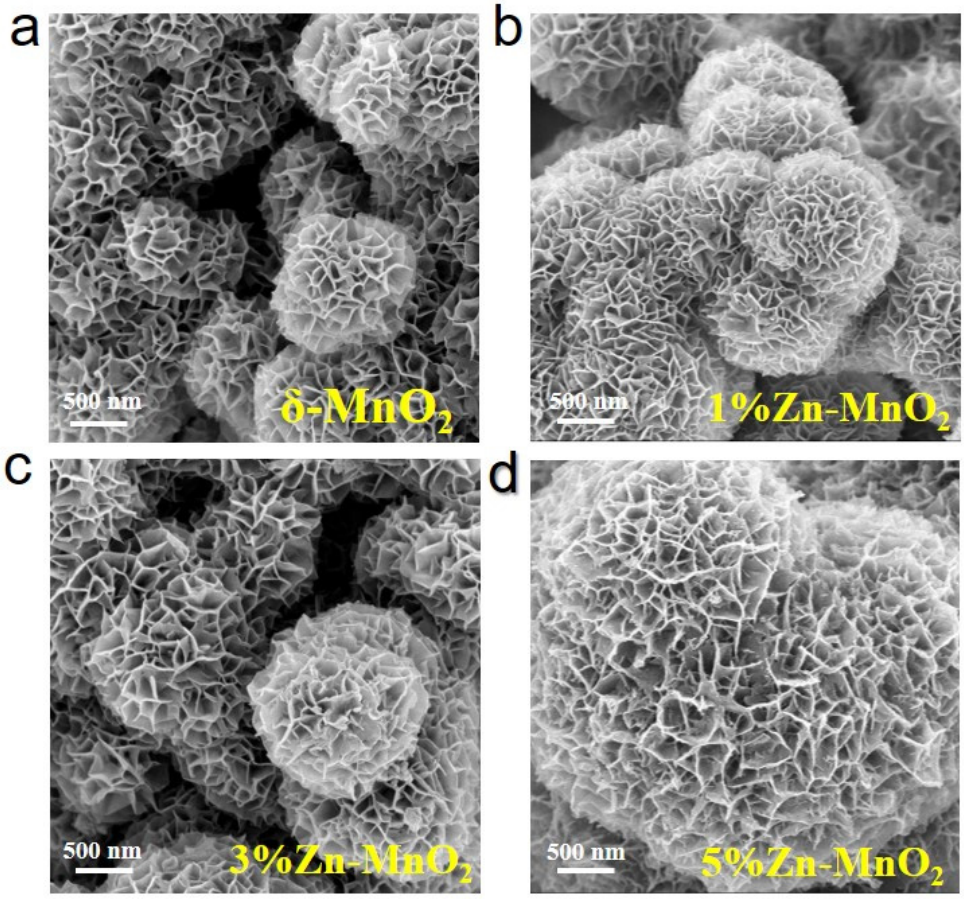

Figure S1. SEM images of samples: (**a**) δ-MnO_2. (**b**) 1%Zn-MnO_2. (**c**) 3%Zn-MnO_2 and (**d**) 5%Zn-MnO_2.

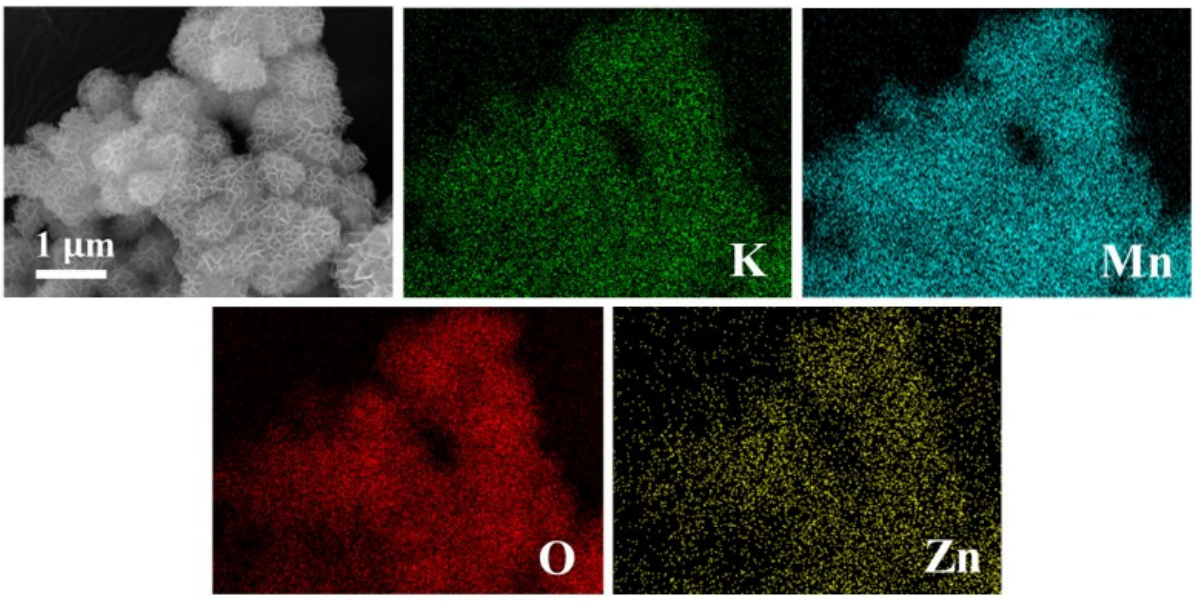

Figure S2. EDS mappings of the Zn-MnO_2 electrode.

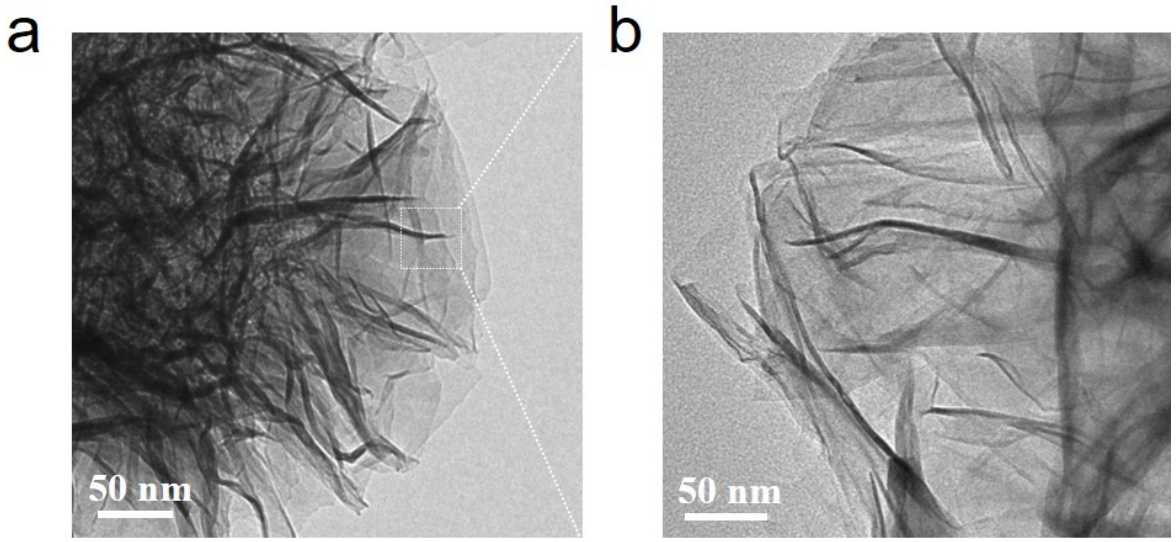

Figure S3. TEM and images of (**a**) δ-MnO_2 and (**b**) Zn-MnO_2.

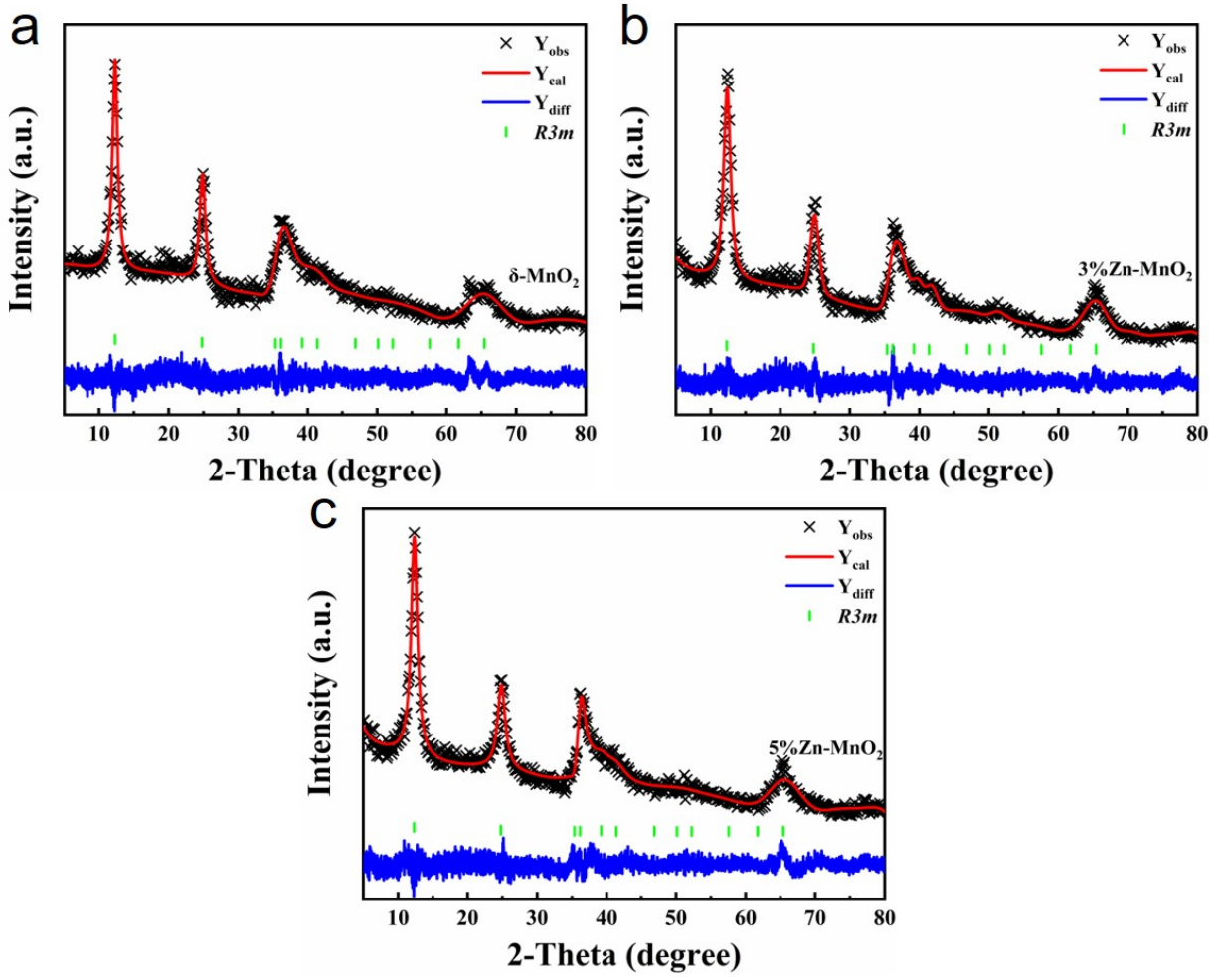

Figure S4. (**a** – **c**) Rietveld refined XRD results of δ-MnO_2, 3% Zn-MnO_2 and 5% Zn-MnO_2.

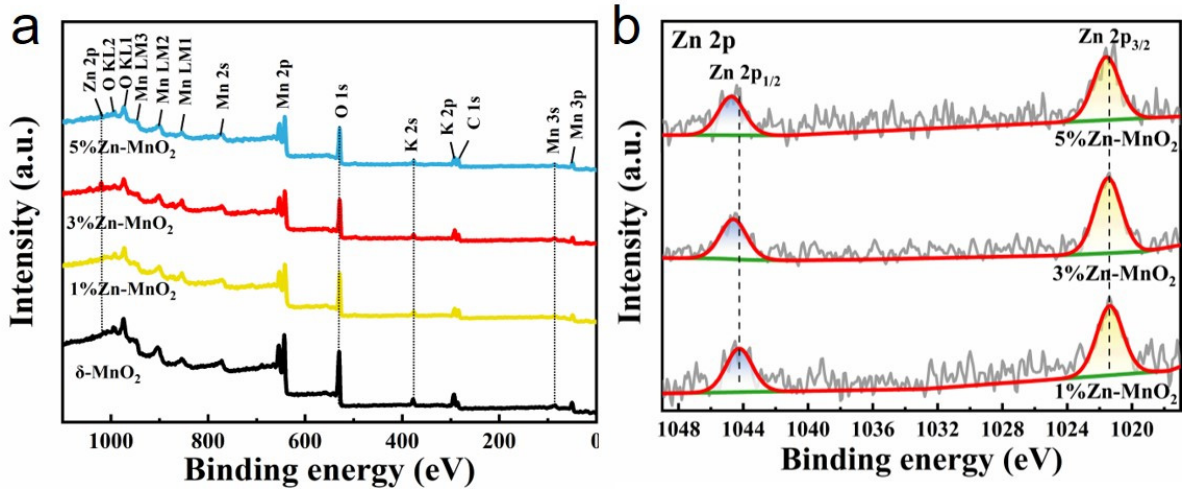

Figure S5. XPS spectra of δ-MnO_2 and C-Zn-MnO_2 (**a**) Full spectrum and (**b**) Zn 2p.

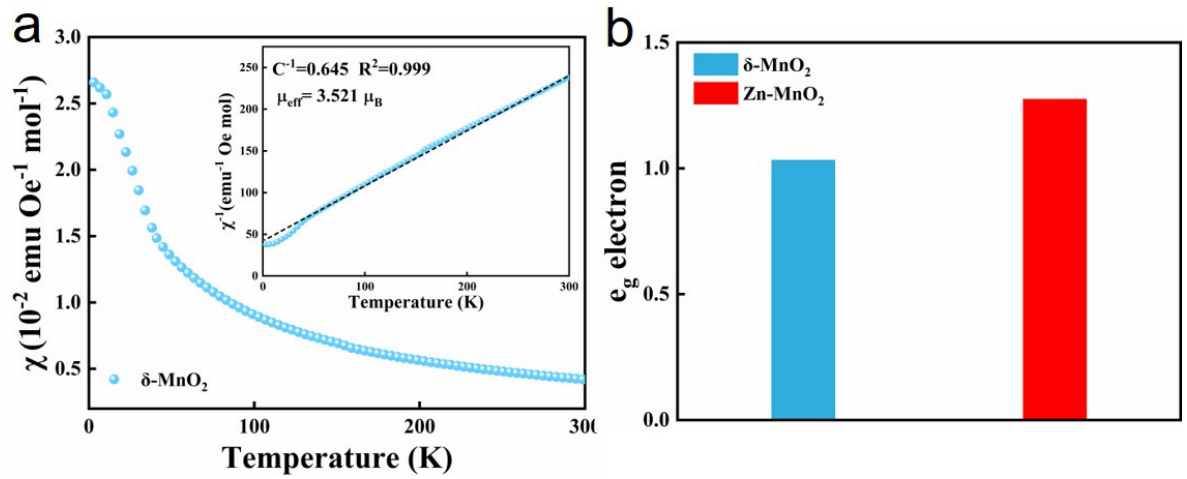

Figure S6. (**a**) Magnetic susceptibility curve of δ-MnO_2 (insert: the plot of inverse susceptibility vs. temperature). (**b**) Calculated e_g filling for δ-MnO_2 (blue) and Zn-MnO_2 (red).

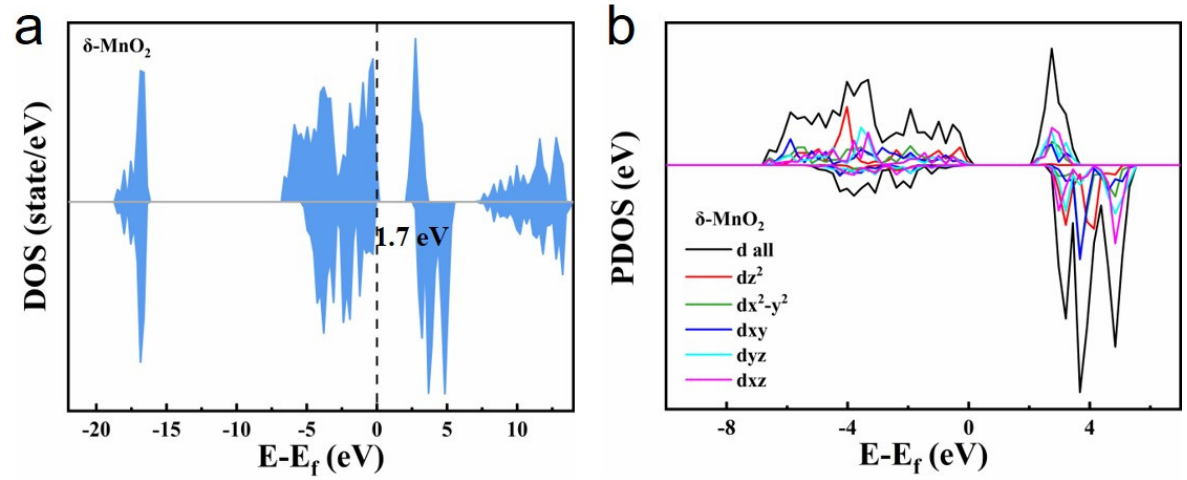

Figure S7. (**a**) DOS of the δ-MnO_2. (**b**) The PDOS of different Mn 3d orbitals in δ-MnO_2.

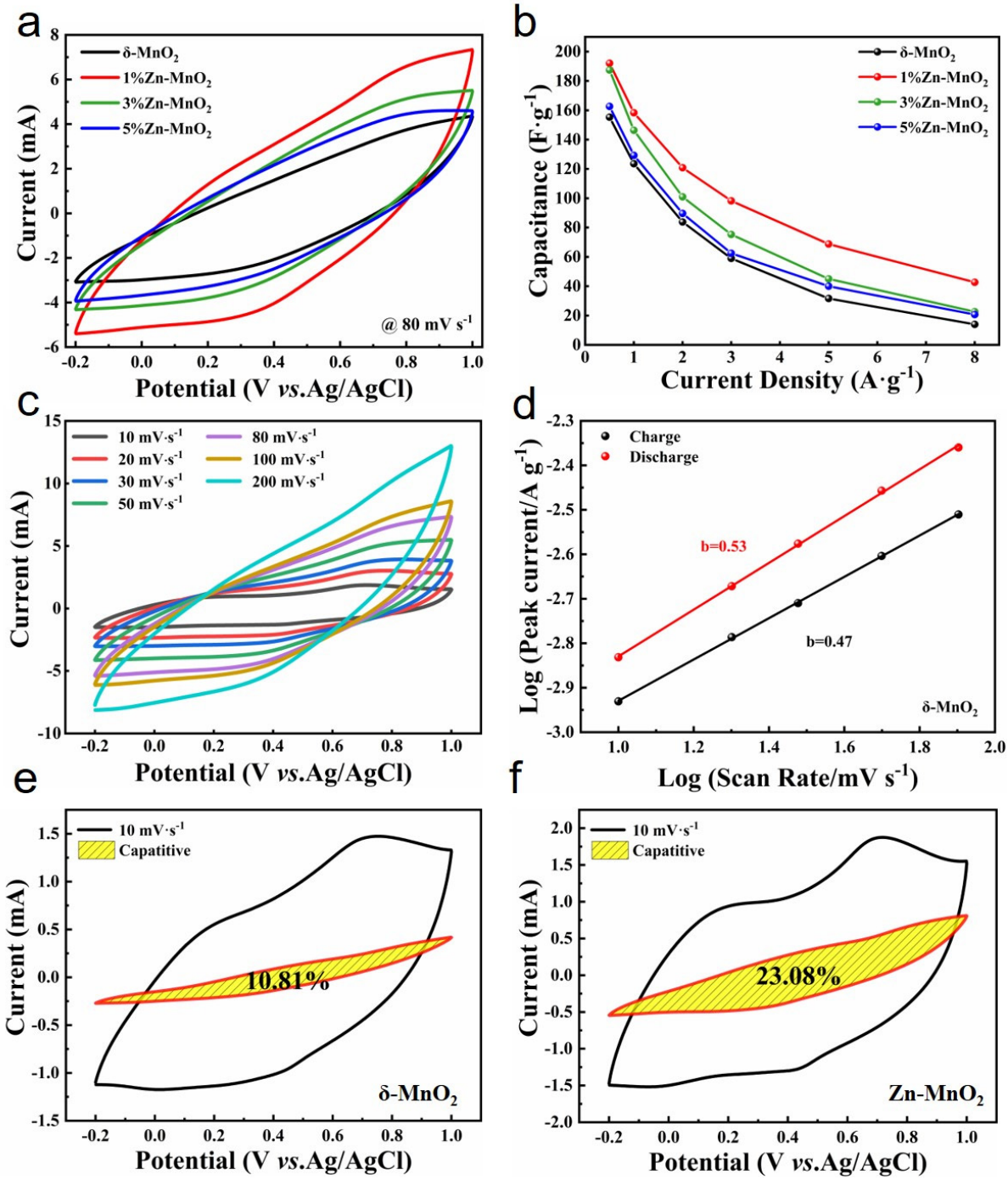

Figure S8. (**a**) CV curves of δ-MnO_2 and C-Zn-MnO_2 at 80 mV s^{-1}. (**b**) The rate capability of δ-MnO_2 and C-Zn-MnO_2. (**c**) CV curves of Zn-MnO_2 at different scanning rates; (**d**) Power law relationship of δ-MnO_2 electrode at different scanning rates; Separation of the capacitive current (shaded region) and diffusion current in (**e**) δ-MnO_2 and (**f**) Zn-MnO_2 at a scan rate of 10 mV s^{-1}.

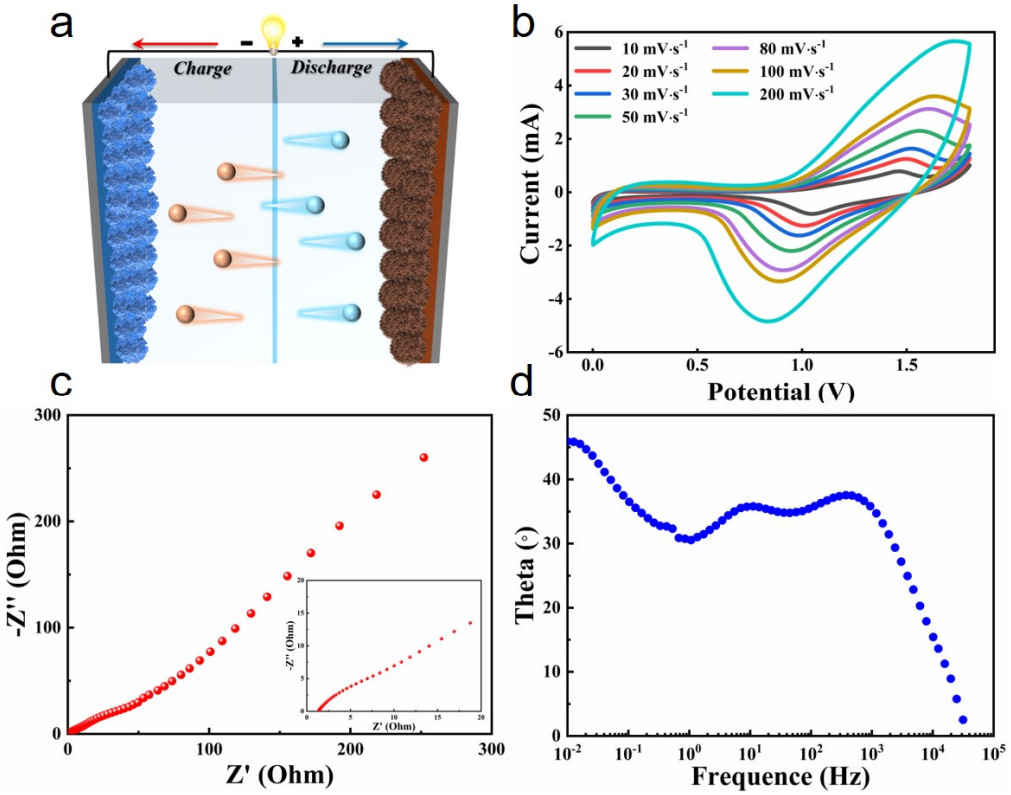

Figure S9. (**a**) Schematic illustration of the device. (**b**) CV curves at scan rate from 10 to 200 mV s^{-1}. (**c**) Nyquist plots (insert: high frequency magnification). (**d**) Bode-phase plots.

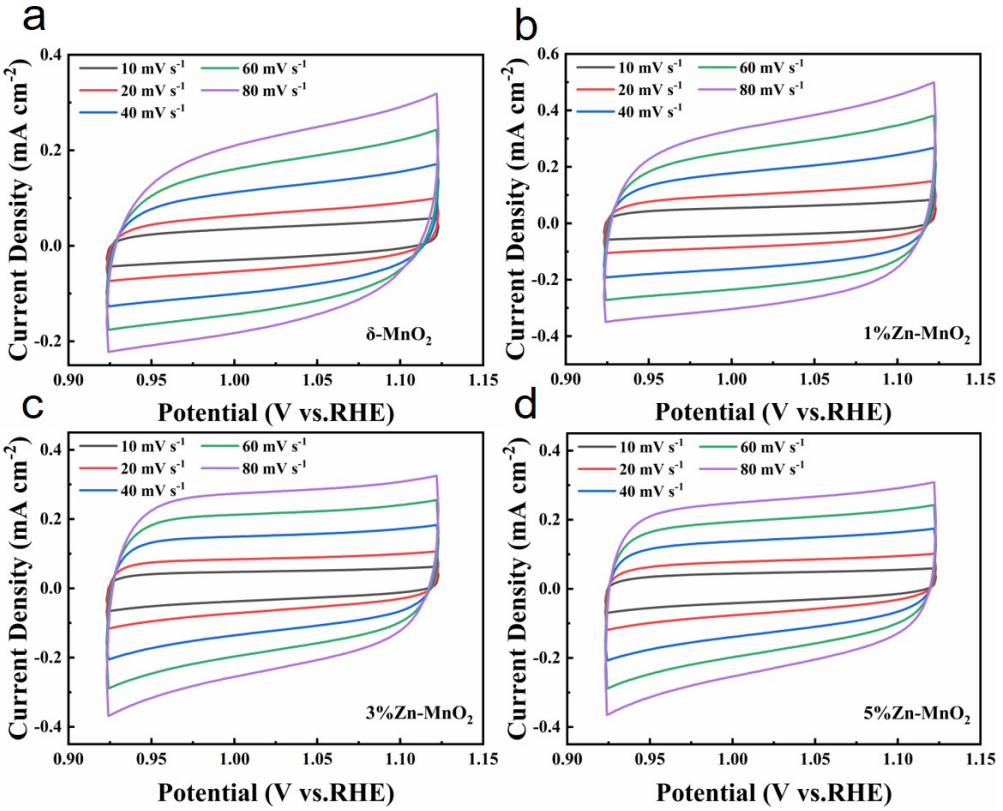

Figure S10. CV curves of (**a**) δ-MnO_2, (**b**) 1%Zn-MnO_2, (**c**) 3%Zn-MnO_2 and (**d**) 5%Zn-MnO_2.

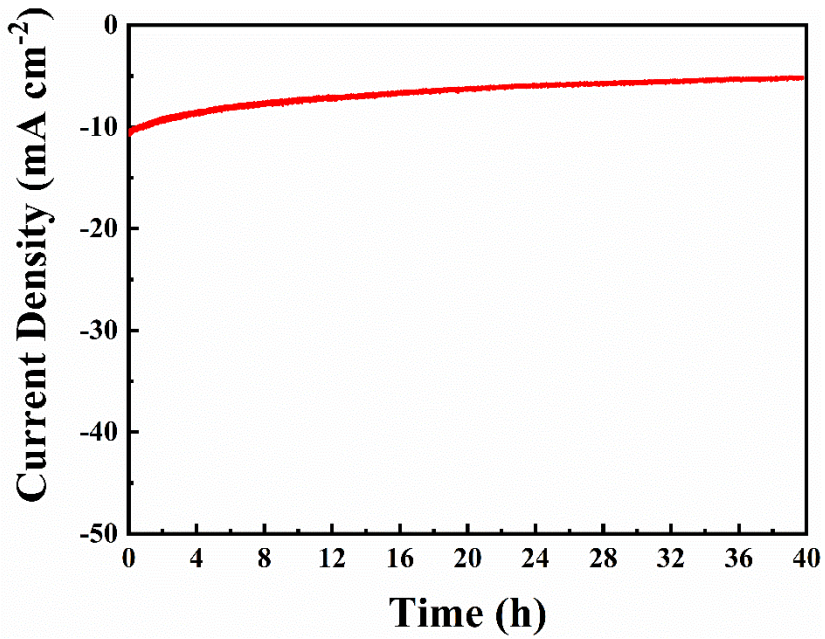

Figure S11. Electrocatalytic stability of Zn-MnO_2 electrode (η = 10 mA cm^{-2}).

Table S1. The crystal data and refinement factors obtained from the XRD result of C-Zn-MnO_2 samples.

Samples	δ-MnO_2	1%Zn-MnO_2	3%Zn-MnO_2	5%Zn-MnO_2
Space group	$R\bar{3}m$	$R\bar{3}m$	$R\bar{3}m$	$R\bar{3}m$
a (Å)	2.84994	2.91439	2.92247	2.93203
b (Å)	2.84994	2.91439	2.92247	2.93203
c (Å)	21.38892	21.32894	21.34527	21.42037
V(Å^3)	150.450	156.890	157.882	159.475
α (°)	90	90	90	90
β (°)	90	90	90	90
γ (°)	120	120	120	120
S (%)	0.13	0.08	0.32	0.48
R_{wp} (%)	9.05	8.44	8.34	8.34
R_p (%)	7.00	6.56	6.39	6.38
χ^2	3.52	3.40	3.41	3.36

Table S2. The fitted parameter based on Curie-Weiss law in related paramagnetic data area for samples.

Samples	C	μ_{eff}	V_{HS}	e_g
δ-MnO_2	1.550	3.521	0.516	1.032
Zn-MnO_2	1.912	3.911	0.637	1.274

Table S3. Integral area of the 3d-orbitals of Mn and the ratio of d-electron spin states in MnO_2 and Zn-MnO_2.

Samples	e_g		t_{2g}				
	d_{z^2}	$d_{x^2-y^2}$	d_{xy}	d_{yz}	d_{yz}	d_{all}	e_g/d_{all} (%)
δ-MnO_2	33.19	34.53	34.56	34.98	34.93	172.91	39.16
Zn-MnO_2	33.84	34.43	34.42	34.83	34.80	172.34	39.61

Table S4. Equivalent circuit fitting impedance results for supercapacitor tests.

Samples	R_s (Ω)	R_{ct} (Ω)	R_{cl} (Ω)
δ-MnO_2	0.57	2.15	123.10
1% Zn-MnO_2	0.56	1.74	45.86
3% Zn-MnO_2	0.48	1.80	62.19
5% Zn-MnO_2	0.67	1.82	87.59

Table S5. Comparison of electrochemical performance of MnO_2-based SCs reported in literature.

Devices	Voltage (V)	Eletrolyte	Energy Density ($Wh \cdot kg^{-1}$)	Power Density ($W \cdot kg^{-1}$)	Ref.
Zn-MnO_2//La-MoO_3/GQD	0~1.8	1 M Li_2SO_4	23.9	450	This work
PI/20%$KMnO_4$–800	0~1.0	6 M KOH	11.4	250	[5]
Mn_3O_4@MnO_2/C	0~1.0	6 M KOH	21.0	250	[5]
MnO_2/Co_2CH@C//AC	0~1.7	PVA-KOH	15	255	[6]
CC-MnO_2//PSC	0~1.8	1 M Na_2SO_4	22.5	237	[7]

Table S6. Impedance fitting results for HER tests.

Samples	R_s (Ω)	R_{ct} (Ω)
δ-MnO_2	1.62	15.62
1%Zn-MnO_2	1.58	4.97
3%Zn-MnO_2	1.56	5.76
5%Zn-MnO_2	1.56	7.16

Table S7. Literature data on HER activity of MnO_2-based electrocatalysts.

Catalysts	Electrolyte	Tafel Slope ($mV\ dec^{-1}$)	η(mV)@*j* ($mA\ cm^{-2}$)	Ref.
NS-MnO_2	1 M KOH	62	167@10	[2]
Co-doped MnO_2 NSs	1 M KOH	122	218@10	[8]
Al-MnO_2	1 M KOH	148	170@10	[9]
rGO/MnO_2/MoS_2	1 M KOH	75.13	205@10	[10]
MnO_2	1 M KOH	135	269@10	[11]
Zn-MnO_2	1 M KOH	85	161@10	This work

References

1. Zhang, X.; Zhang, F.; Wei, D.; et al. Design and synthesis of K-doped tremella-like δ-MnO_2 for high-performance supercapacitor. *J. Energy Storage* **2023**, *72*, 108468. https://doi.org/10.1016/j.est.2023.108468.
2. Zhao, Y.; Chang, C.; Teng, F.; et al. Defect-Engineered Ultrathin δ-MnO_2 Nanosheet Arrays as Bifunctional Electrodes for Efficient Overall Water Splitting. *Adv. Energy Mater.* **2017**, *7*, 1700005. https://doi.org/10.1002/aenm.201700005.
3. Gao, Z.; Zhao, Z.-h.; Wang, H.; et al. Jahn–Teller Distortions Induced by in situ Li Migration in λ-MnO_2 for Boosting Electrocatalytic Nitrogen Fixation. *Angew. Chem. Int. Ed.* **2024**, *63*, e202318967. https://doi.org/10.1002/anie.202318967.
4. Zhang, Z.; Zheng, J.; Chen, X.; et al. Achieving ultra-long cycling life for MnO_2 cathode: Modulating Mn^{3+} spin state to suppress Jahn–Teller distortion and manganese dissolution. *Energy Storage Mater.* **2025**, *76*, 104128. https://doi.org/10.1016/j.ensm.2025.104128.
5. Wang, H.; Wang, Y.; Sun, J.; et al. Needle-like nanostructured Mn_3O_4@MnO_2/C composites with boosted electrochemical performance as high-performance supercapacitor electrodes. *J. Electroanal. Chem.* **2025**, *992*, 119279. https://doi.org/10.1016/j.jelechem.2025.119279.
6. Zhang, A.; Mao, N.; Zhong, Y.; et al. Synthesis of petaloid and origami-lantern shaped MnO_2/Co_2CH@C hierarchical core-shell nanorod arrays for portable asymmetric supercapacitor. *Compos. Part B Eng.* **2021**, *215*, 108756. https://doi.org/10.1016/j.compositesb.2021.108756.
7. Zheng, X.; Liu, X.; Yang, X.; et al. Templating preparation of cannular congeries of MnO_2 and porous spheres of carbon and their applications to high performance asymmetric supercapacitor and lithium-sulfur battery. *Colloids Surf. A Physicochem. Eng. Asp.* **2021**, *610*, 125740. https://doi.org/10.1016/j.colsurfa.2020.125740.
8. Patra, P.; Laha, S.; Ghosh, S. Exfoliated Cobalt-Doped Manganese Oxide Nanosheets: An Efficient and Stable Electrocatalyst for Hydrogen Evolution Reaction in an Alkaline Medium. *ACS Appl. Energ. Mater.* **2024**, *7*, 3577–3589. https://doi.org/10.1021/acsaem.3c03022.
9. Sun, H.; Chen, S.; Zhang, B.; et al. Cation-doped sea-urchin-like MnO_2 for electrocatalytic overall water splitting. *Dalton Trans.* **2023**, *52*, 17407–17415. https://doi.org/10.1039/D3DT03059H.
10. Denisdon, S.; Senthil Kumar, P.; Boobalan, C.; et al. Hydrothermally Synthesized rGO/MnO_2/MoS_2 Nanohybrids as Superior Bifunctional Electrocatalysts for Oxygen and Hydrogen Evolution Reactions. *Langmuir* **2024**, *40*, 17753–17766. https://doi.org/10.1021/acs.langmuir.4c02192.
11. Wei, J.-X.; Cao, M.-Z.; Xiao, K.; et al. In Situ Confining Pt Clusters in Ultrathin MnO2 Nanosheets for Highly Efficient Hydrogen Evolution Reaction. *Small Struct.* **2021**, *2*, 2100047. https://doi.org/10.1002/sstr.202100047.